Conference on Modelling Fluid Flow (CMFF'25)
The 19th International Conference on Fluid Flow Technologies
Budapest, Hungary, August 26-August 29, 2025

A NOVEL EULERIAN-LAGRANGIAN MULTI-SCALE METHOD FOR CAVITATING FLOW IN AN INJECTOR NOZZLE

Wei Guan[1], Shengnan Zhang[2], Chuqiao Wang[3], Zhixia He[2], Dominique Thévenin[1]

[1] Corresponding Author. Lab. of Fluid Dynamics and Technical Flows, University of Magdeburg "Otto von Guericke", Magdeburg 39106, Germany. E-mail: wei.guan@ovgu.de
[2] Institute for Energy Research, Jiangsu University, Zhenjiang, PR China
[3] School of Energy and Power Engineering, Jiangsu University, Zhenjiang, PR China

ABSTRACT

The cavitation phenomena found in high-pressure fuel injector nozzles have a significant influence on the performance of subsequent spray mixing, combustion, and even emissions in internal combustion engines. In particular, cloud cavitation accompanied by complex interactions between phase transition and turbulent fluctuations induced by the shedding of vapor bubbles, inevitably results in nozzle wall erosion while facilitating the primary breakup of the liquid jet. The in-nozzle cavitating flow is generally captured by using an Eulerian method coupled with large eddy simulation (LES). However, this approach cannot capture the behavior of vapor bubbles at scales smaller than the LES grid. Therefore, an Eulerian-Lagrangian multiscale model is proposed here to simulate the multiscale vapor structure in a scaled-up injector nozzle. The Volume of Fluid (VOF) method is employed to capture the macroscopic characteristics of cavitation, while a Lagrangian method is used to track microscopic bubbles. This combined Eulerian-Lagrangian approach leads to a two-way coupling and reveals the mechanisms controlling cavitation bubble shedding in the nozzle. It accurately reproduces the multiscale features of cavitation, in particular the evolution of large cavities as well as the dynamic characteristics of microscopic bubbles. The results indicate that shedding cycles of cavitation cloud are mainly induced by the re-entrant jet for a cavitation number below 1.64.

Keywords: Injector nozzle, Multi-scale cavitation, Eulerian-Lagrangian model, Re-entrant jet

1. INTRODUCTION

Atomizing liquid jets are utilized across various fields, including medical sprays, rocket engines, and internal combustion engines. In recent decades, numerous studies have focused on enhancing atomization performance in diverse industrial applications, with fuel injection spray processes in internal combustion engines (ICE) being a typical example. Outstanding fuel injection atomization can significantly enhance engine combustion efficiency and reduce emissions [1, 2]. Furthermore, the internal flow behavior within the injector, particularly in the presence of cavitation, has a significant influence on fuel spray characteristics, highlighting the need for a thorough understanding of nozzle cavitating flow [3, 4].

With its tiny geometric scale (~0.1 mm diameter), high injection pressure (>160 MPa), and extremely short injection duration (~3 ms), the nozzle orifice exhibits micro-scale, ultra-high-speed, strongly transient, and highly turbulent internal flow characteristics. The abrupt change in the flow cross-section at the orifice entrance causes the fuel to detach from the wall, resulting in a significant depressurization. When the local pressure drops below the saturation vapor pressure of the fuel, cavitation occurs, causing the fuel to transition from liquid to gas phase and resulting in a complex two-phase cavitating flow within the nozzle. Moreover, shear and vortex flows within the nozzle induce various forms of cavitation, increasing the complexity of the internal flow.

While cavitation within the injector nozzle can enhance jet breakup and improve atomization, it may also reduce orifice flow capacity and cause cavitation erosion, potentially leading to injector failure [5]. Cavitation induces complex flow issues [6], including shock waves and turbulent vortices, and associated effects such as pressure fluctuations, vibrations, and noise [7, 8], all of which have attracted considerable attention in fields such as fluid machinery and fuel injection system. The pressure fluctuations and pulses generated by cavitation are major contributors to pipeline system corrosion [9, 10]. Accordingly, the study of shock wave propagation is essential for gaining a deeper understanding of the mechanisms underlying cavitation bubble growth and collapse. This phenomenon typically occurs during the final stage of cavity collapse, taking place on ex-

tremely small temporal and spatial scales and characterized by the dynamic behavior of a cloud of discrete bubbles and minute mixed-phase cavities.

Nonetheless, accurately capturing the dynamic characteristics of discrete cavities remains a significant challenge. The commonly used homogeneous mixture models within the Eulerian framework effectively capture large cavities but fail to accurately represent smaller cavities that are below the grid resolution. A potential solution is a multi-scale hybrid model, where macro-scale cavity structures are captured using a homogeneous mixture approach, such as the Volume of Fluid (VOF) method with a mass transfer model, while micro-scale cavity structures are modeled using a Lagrangian approach, governed by the Newtonian motion of individual spherical bubbles and by the Rayleigh–Plesset equation for bubble dynamics [11, 12]. In the present work, therefore, a Eulerian–Lagrangian multi-scale cavitation model is employed, in order to investigate cavitation shedding mechanisms induced by shock waves. Coupled to LES simulations, the micro-bubbles performance is obtained in an injector nozzle for different shedding mechanisms.

2. NUMERICAL METHODOLOGY

2.1. VOF method

The VOF method has been utilized for the simulation of cavitating flows in the injector nozzle. The transport equations for continuity, momentum, and for capturing the macro-scale vapor cavities are as follows

$$\frac{\partial \rho_m}{\partial t} + \nabla \cdot (\rho_m \mathbf{U}) = 0, \quad (1)$$

$$\frac{\partial (\rho_m \mathbf{U})}{\partial t} + \nabla \cdot (\rho_m \mathbf{U}\mathbf{U}) = -\nabla p + \nabla \cdot \tau - \vec{F_B}, \quad (2)$$

$$\frac{\partial (\alpha_v \rho_v)}{\partial t} + \nabla \cdot (\alpha_v \rho_v \mathbf{U}) = \dot{R}_e - \dot{R}_c, \quad (3)$$

where ρ_m, ρ_v, $\mathbf{U}$, and p are the mixture density, vapor density, velocity, and pressure, respectively. The viscous stress tensor τ is defined as $\tau = \mu\left(\nabla\mathbf{U} + (\nabla\mathbf{U})^{\mathrm{T}}\right) + \boldsymbol{\tau}_t$, where μ is the mixture viscosity and $\boldsymbol{\tau}_t$ is the turbulent stress. Here, α_v is the volume fraction of vapor, and therefore the volume fraction of liquid is defined as $\alpha_l = 1-\alpha_v$. The source term $\dot{R}_e - \dot{R}_c$ is the phase change mass transfer rate between the liquid and vapor, calculated by using the Zwart–Gerber–Belamri (ZGB) [13] cavitation model in this work. The source terms are given by

$$\dot{R}_e = F_{vap} \frac{3\alpha_{\mathrm{nuc}}(1-\alpha_v)\rho_v}{R_{\mathrm{B}}} \sqrt{\frac{2}{3}\frac{(p_v - p)}{\rho_l}}, \quad p \le p_v, \quad (4)$$

$$\dot{R}_c = F_{\mathrm{cond}} \frac{3\alpha_v \rho_v}{R_{\mathrm{B}}} \sqrt{\frac{2}{3}\frac{(p - p_v)}{\rho_l}}, \quad p > p_v, \quad (5)$$

where F_{vap} and F_{cond} are empirical coefficients, respectively. R_{B} represents the mean radius of bubbles, which is assumed to be 0.001 mm in this model, while α_{nuc} is the nucleation site volume fraction, which is fixed at 0.0005. Considering that the focus of the paper is to resolve cloud cavitation at normal fuel operating temperature within the injection orifice, where the variation of temperature does not vary more than 10 K for the pressure drops considered, the isothermal assumption has been adopted in the present study. Therefore, the energy conservation equation is not considered in the barotropic behavior of the fluid in this work.

2.2. Discrete bubble model

The discrete bubble model (DBM) within the Lagrangian framework for tracing bubbles on the coarse-grid domain is given by

$$\vec{u_{\mathrm{B}}} = \frac{dx}{dt}, \quad (6)$$

$$M_{\mathrm{B}} \frac{d\vec{u_{\mathrm{B}}}}{dt} = \vec{F}_{\mathrm{Drag}} + \vec{F}_{\mathrm{VM}} + \vec{F}_{\mathrm{PG}}, \quad (7)$$

where M is the mass and subscript B represents discrete bubbles, while $\vec{F}_{\mathrm{Drag}}$, $\vec{F}_{\mathrm{VM}}$, $\vec{F}_{\mathrm{PG}}$ are the drag force, the virtual-mass force, and the pressure gradient force, respectively, calculated using the following equations

$$\vec{F}_{\mathrm{Drag}} = M_{\mathrm{B}} \frac{\vec{u} - \vec{u_{\mathrm{B}}}}{\tau_r}, \quad (8)$$

$$\vec{F}_{\mathrm{VM}} = C_{\mathrm{VM}} M_{\mathrm{B}} \frac{\rho_m}{\rho_v}\left(\vec{u}_{\mathrm{B}} \nabla \vec{u} - \frac{d\vec{u_{\mathrm{B}}}}{dt}\right), \quad (9)$$

$$\vec{F}_{\mathrm{PG}} = \frac{\rho_m}{\rho_v} M_{\mathrm{B}} \vec{u}_{\mathrm{B}} \nabla \vec{u}, \quad (10)$$

where C_{VM} is the virtual-mass force coefficient taken equal to 0.5. The quantity τ_r is the relaxation time of discrete bubbles, given by

$$\tau_r = \frac{\rho_v d_{\mathrm{B}}^2}{3\mu_m} \frac{4}{C_d \mathrm{Re}}, \quad (11)$$

where C_d is the drag coefficient calculated by the spherical drag law, and Re is the relative Reynolds number, calculated by the following formula

$$\mathrm{Re} = \frac{\rho_m d_{\mathrm{B}} \left|\vec{u}_{\mathrm{B}} - \vec{u}\right|}{\mu_m}. \quad (12)$$

The integral average in each control volume is expressed as

$$\vec{F}_{\mathrm{B}} = -\frac{1}{V_{\mathrm{cell}}} \sum_{i=1}^{N} \left(\vec{F}_{\mathrm{Drag},i} + \vec{F}_{\mathrm{VM},i} + \vec{F}_{\mathrm{PG},i}\right), \quad (13)$$

where the subscript i represents the bubbles in the control volume. This study employs a simplified Rayleigh–Plesset equation to simulate the growth and collapse of discrete bubbles, leading to

$$\frac{\mathrm{d}R_{\mathrm{B}}}{\mathrm{d}t} = sign(p_v - p)\sqrt{\frac{2}{3}\left|\frac{p_v - p}{\rho_l}\right|}, \quad (14)$$

where R_B is the radius of discrete bubbles with an initial value of 1×10^{-6} m. Since the above equation only considers the first-order term of the Rayleigh–Plesset equation and neglects the second-order term and surface tension, two coefficients C_v and C_c are introduced to correct the growth and collapse rates of the bubbles. Because bubbles are not only produced in parts below the saturation vapor pressure, a nucleation coefficient C_{csp} which is greater than 1 is also introduced, referred to as the nucleation pressure. The growth and collapse of the bubbles can be expressed as

$$\frac{dR_B}{dt} = \begin{cases} C_v \sqrt{\frac{2}{3}\left(C_{csp}p_v - p\right)/\rho_l}, & p \le C_{csp}p_v \\ C_c \sqrt{\frac{2}{3}\left(p - C_{csp}p_v\right)/\rho_l}, & p \ge C_{csp}p_v \end{cases} \quad (15)$$

where C_v, C_c, and C_{csp} are 0.5, 0.01, and 1.2, respectively, as suggested by Li et al. [14]. To simulate the nucleation process, nuclei are randomly injected into the region where the local pressure is lower than the nucleation pressure. Nuclei are allocated with a number of nucleation sites per unit cell volume set to 1×10^{10} m^{-3}.

2.3. Multiscale transformation algorithm

A discrete-continuum transformation algorithm is employed for multiscale modeling of cavitation bubbles across different fluid scales. During fuel injection in the nozzle, large-scale cavities are well-resolved with high grid resolution in LES simulations, enabling the accurate capture of cavity shedding. Sub-grid scale cavities are converted into Lagrangian bubbles, initiating the transition from VOF to DBM, as presented in Figure 1a. When $p_{csp}p_{sat} \leqslant p$ and $\alpha_v < 0.6$ are satisfied simultaneously in one grid cell, the Eulerian cavity within the grid cell is replaced by an equivalent volume of discrete bubbles, triggering the VOF-to-DBM transition.

Nonetheless, when the volume of discrete bubble touches the liquid-vapor interface and the volume fraction of vapor phase exceeds 0.6, further tracking by the DBM is deemed unacceptable. Therefore, two transition modes are considered in this work to achieve the transition from DBM to VOF. The first mode involves the coalescence between the DBM and VOF methods, as shown in Fig. 1b. The second mode represents the transition from DBM to VOF due to the growth of discrete bubbles, as illustrated in Fig. 1c. When a discrete bubble reaches the liquid-vapor interface, the transition depends on the volume ratio of the bubble V_B to the grid cell volume V_{cell}. If $V_B/V_{cell} < 1 - \alpha_v$, the discrete bubble is incorporated into the Eulerian cavity for further calculation, and the gas phase volume fraction in the grid cell is updated as $\alpha_v = \alpha_v + V_B/V_{cell}$. Conversely, if $V_B/V_{cell} \geqslant 1 - \alpha_v$, the vapor volume fraction with the grid cell reaches $\alpha_v = 1$, and the excess bubble volume beyond the grid cell capacity is evenly distributed among the neighboring cells, thereby achieving the DBM-to-VOF conversion. During the transition, the Lagrangian framework removes the bubble and transfers its mass into the VOF simulation. Accordingly, a source term should be incorporated into the volume-fraction equation of the vapor [14], expressed as follows

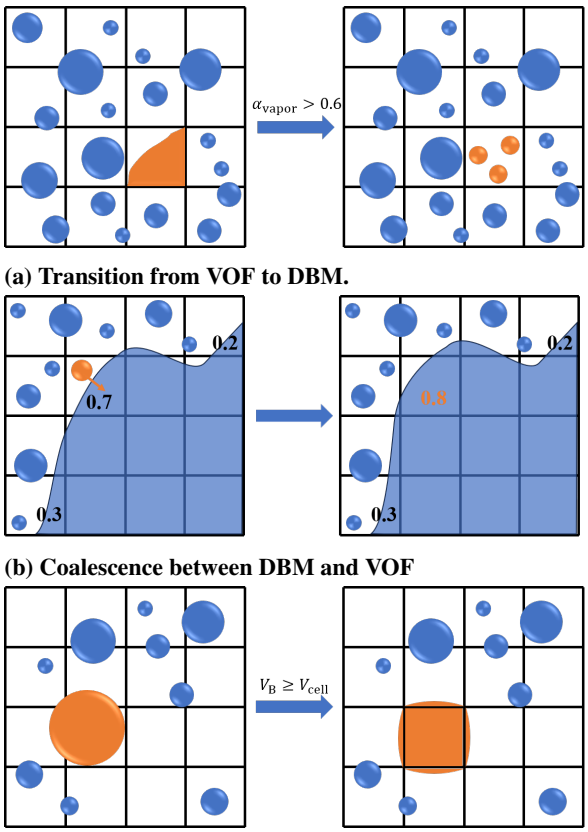

(a) Transition from VOF to DBM.

(b) Coalescence between DBM and VOF

(c) Transition from DBM to VOF.

Figure 1. Diagram of VOF-DBM with two-way transition.

$$\frac{\partial(a_v\rho_v)}{\partial t} + \nabla \cdot (a_v\rho_v \mathbf{U}) = \dot{R}_e - \dot{R}_c + S_B, \quad (16)$$

where S_B represents the source due to the transition from discrete bubbles (DBM) to macro-scale cavities (VOF), which is expressed as follow

$$S_B = \begin{cases} \frac{\rho_v V_B}{V_{cell}\Delta t} & \text{if bubble is removed} \\ 0 & \text{else} \end{cases} \quad (17)$$

2.4. Turbulence modeling

The LES model employs a spatial low-pass filter operation determined by the cell size of the computational domain to separate the eddies at different scales. In this study, for modeling the unresolved turbulence, the Wall-Adapting Local Eddy-Viscosity (WALE) model is employed [15]. The sub-grid scale model (SGS) turbulent closure is defined as

$$\tau_t = \frac{1}{3}\tau_{kk}\delta_{ij} - 2\mu_t\overline{S}_{ij}, \quad (18)$$

where $\overline{S}_{ij}$ is the rate of strain tensor for the resolved scale. τ_{kk} is the isotropic part that is not modeled but added to the filtered static pressure term, while μ_t is the sub-grid-scale turbulent viscosity given as

$$\mu_t = \rho L_s^2 \frac{(\mathbf{S}_{ij}^d \mathbf{S}_{ij}^d)^{3/2}}{(\mathbf{S}_{ij}^d \mathbf{S}_{ij}^d)^{5/4} + (\bar{\mathbf{S}}_{ij} \bar{\mathbf{S}}_{ij})^{5/2}}, \tag{19}$$

where L_s is the length scale based on the cell volume V_{cell} and the distance to the closest wall d.

2.5. Case setup

The geometry of the computational domain is illustrated in Fig. 2. The geometrical topology of the rectangular nozzle is derived from a previous study [16]. The width W and length L of the nozzle are about 2 and 4 mm, respectively. The nozzle has a W/L ratio of 2 and a nominally sharp entrance. This structure can be representative for cavitating flow in fuel injectors, since the velocities and cavitation obtained are similar to the large-scaled fuel injector nozzle and it is easy to investigate cloud cavitation.

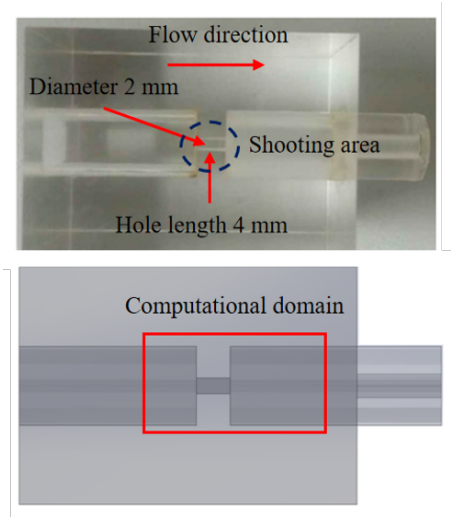

Figure 2. Transparent nozzle geometry.

For a LES simulation, a sufficient mesh resolution is essential for capturing the large-scale turbulent structure. Therefore, a proper balance between computational accuracy and computational cost is required, which is favored by a suitable arrangement of the computational domain grid. The Taylor microscale (λ_g) from the statistical theory of turbulence is used as a common guideline for selecting the LES mesh in the relevant literature [4, 17]

$$\lambda_g = \sqrt{10}\text{Re}^{-0.5} D_{\text{out}} \approx 65\mu\text{m}, \tag{20}$$

The mesh is refined near the walls and the inlet sharp edge as shown in Fig. 3. The minimum cell size near the wall is 2 µm and the maximum dimensionless wall distance (y^+) in the area of interest is about 1.

In this study, simulations were conducted for a

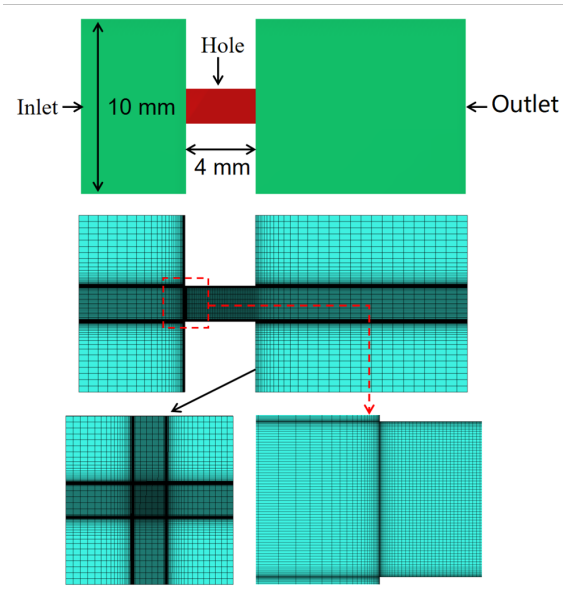

Figure 3. Computational mesh.

cavitation number $\sigma = 1.64$ to investigate the shedding behavior of unsteady cavitation. The cavitation number of the nozzle is defined as

$$\sigma = \frac{p_{\text{in}} - p_{\text{sat}}}{p_{\text{in}} - p_{\text{out}}} \tag{21}$$

where p_{in} and p_{sat} are the inlet pressure and the saturation pressure, and p_{out} is the fixed outlet pressure of 101325 Pa.

The employed solver is the segregated, pressure-based formulation in the ANSYS Fluent platform (Version 18.0). User-defined functions (UDFs) are implemented to achieve the development of DBM for cavitation and the combination between DBM and VOF. The pressure–velocity coupling scheme relies on the PISO scheme. The cell gradients are calculated using Least Square Cell Based method. The pressure interpolation is performed using the body force weighted scheme due to its robustness. The convective terms for the momentum are discretized using a bounded central differencing scheme. Finally, the time integration has been performed by adopting a bounded second-order implicit scheme. An adaptive time step is employed based on a Courant–Friedrichs–Lewy (CFL) number. An empirically value of 0.8 is adopted in the present study, limiting the diffusion of turbulent vortex clusters into the flow.

3. RESULTS AND DISCUSSION

3.1. Validation

The numerical results are validated against the experimental observations by He et al [16]. A detailed description of the experimental setup is provided in [16], in which the typical periodic shedding and collapse of cloud cavitation are observed at a cavitation number of $\sigma = 1.64$. To better visualize

the vapor distribution in the flow field, all cases using the VOF-LES and VOF-DBM-LES methods are represented through the iso-surface of the vapor volume fraction at $\alpha_v = 0.1$. Figure 4 shows the transient experimental flow pattern, the VOF-LES simulation results, and the VOF-DBM-LES simulation results.

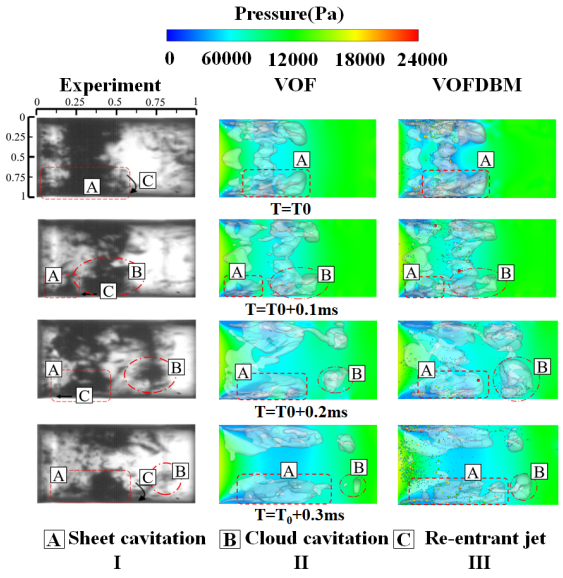

Figure 4. Comparison of simulation results with the experimental data at $\sigma = 1.64$.

As the volume fraction field only captures the macroscopic distribution of the vapor cavity, both simulation results show some discrepancies compared with the experimental results. The results using the VOF-LES method aligns well with the experimental observations in the first two time frames; however, in the latter two, the shed cloud cavitation is noticeably smaller compared to the experiment. Particularly at time frame IV, the cloud cavitation almost entirely collapses, showing a significant deviation from the experimental results. Moreover, this approach fails to capture the development of discrete bubbles during the flow process. In contrast, the VOF-DBM-LES approach not only accurately reproduces the growth of sheet cavitation, the shedding, collapse, and periodic behavior of cloud cavitation observed in the experiment but also provides a clear representation of the development of microscopic bubbles throughout the flow process.

The VOF-DBM method used in this study enables the two-way transition between large-scale cavities and microscopic bubbles, in contrast to the traditional VOF method. The transition occurs when the conversion threshold is reached. To better illustrate the processes of bubble injection, growth, collapse, and two-way transition, all bubbles are magnified by a factor of 3 based on their diameter, as shown in Fig.5. Figure 5(a) shows the injection, growth, and collapse of discrete bubbles over a 3 μs time interval, with different arrows representing different processes. Figures 5(b) and 5(c) illustrate the Lagrangian-to-Eulerian transition, representing different transition mechanisms, which are discussed in Section 2 of this study. Figure 5(d) depicts the

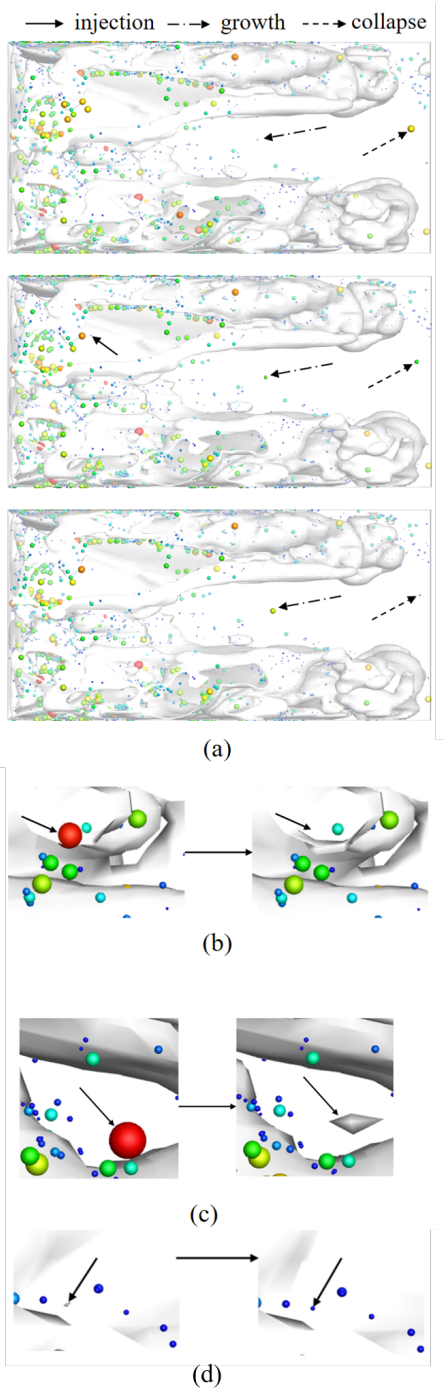

Figure 5. Injection, growth, collapse of discrete bubbles, and the two-way transition between Eulerian and Lagrangian frames: (a) Injection, growth, and collapse of discrete bubbles, (b) Lagrangian-to-Eulerian transition, (c) Lagrangian-to-Eulerian transition, (d) Eulerian-to-Lagrangian transition.

Eulerian-to-Lagrangian transition. The time intervals for Figs.5(b), (c), and (d) are 2 μs.

3.2. Characteristics of cavitation shedding

At $\sigma = 1.64$, the cavitating flow exhibits a periodic process, including the growth of sheet cavitation, the shedding of cloud cavitation, and the collapse of cloud cavitation, as shown in Fig. 6. Once cavitation develops to time t_0, periodic shedding and collapse of cavitation begin to appear in the flow field. The sheet cavitation grows continuously along with the formation of the re-entrant jet, reaching its maximum size at t_0. At this time, the re-entrant jet begins to cut through the sheet cavitation until $t = t_0 + 0.1$ ms. Then, the rear part of the sheet cavitation is severed by the re-entrant jet, leading to a reduction in the length of sheet cavitation, and the detached part immediately forms cloud cavitation. The shed cloud cavitation moves downstream along with the mainstream flow, while the sheet cavitation continues to grow at the point where it was cut off. From $t = t_0 + 0.1$ to $t = t_0 + 0.2$, the sheet cavitation grows, eventually recovering its original length by $t = t_0 + 0.2$, and maintaining a relatively stable state. During this period, small-scale secondary shedding of tiny cavities occasionally occurs from the rear part of the sheet cavitation. At this stage, the re-entrant jet starts forming from the rear of the sheet cavitation and gradually propagates upstream, while the shed cloud cavitation continues to move downstream. Due to the pressure recovery, the cloud cavitation begins to collapse. As the cloud cavitation approaches the nozzle exit at $t = t_0 + 0.3$, the recovered pressure causes the rapid collapse of the cloud cavitation. Finally, at $t = t_0 + 0.4$, the flow field returns to its state at t_0, marking the start of a new cavitation cycle.

Figure 7 shows the $x - t$ diagram of the numerical simulation results at $\sigma = 1.64$. It captures at least one complete cycle of cavitation development. The cavitation structures are represented by the isosurface of vapor volume fraction at $\alpha_v = 0.1$, shown in white, while the background is displayed in black. The green solid line represents the reduction of sheet cavitation, indicating the shedding of cloud cavitation. The yellow solid line represents the growth of sheet cavitation. The blue solid line represents the downstream transport of cloud cavitation with the mainstream flow, while the red dashed line indicates the collapse of cloud cavitation. The shedding type of cloud cavitation can be determined based on the rate of reduction of sheet cavitation, which corresponds to the slope of the green solid line.

As shown in Fig. 7, the cavitation shedding phenomenon exhibits relatively simple characteristics, with only one noticeable instance of sheet cavitation reduction observed. The reduction rate of sheet cavitation is relatively low, at 9.6 m/s, indicating that the cavitation shedding process is slow and stable. Therefore, it can be concluded that, under the conditions of this study, the shedding mechanism of cloud

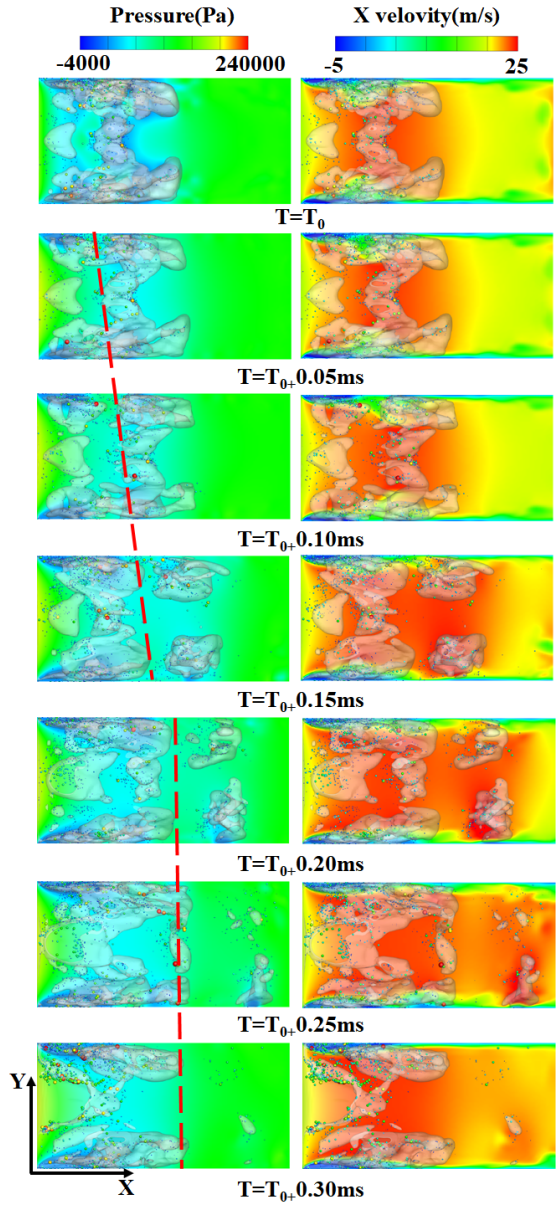

Figure 6. Cloud cavitation shedding and collapse at a cavitation number of $\sigma = 1.64$.

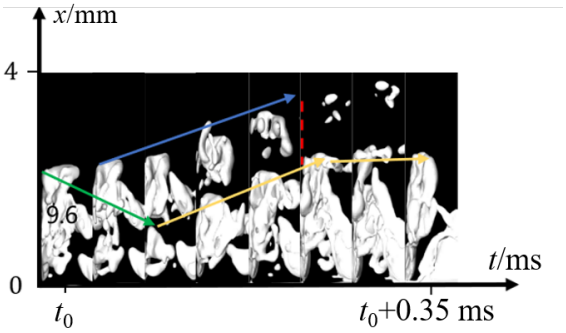

Figure 7. $x - t$ diagram at $\sigma = 1.64$.

cavitation is primarily influenced by the re-entrant jet, with other possible shedding mechanisms playing a negligible role in this process.

4. CONCLUSION

In this study, an Euler-Lagrangian multiscale model is employed to simulate the cavitation process in the nozzle, with a focus on the cavitation shedding mechanism. The VOF method is used to simulate the macroscopic cavity characteristics, while the Lagrangian method is applied to solve for the small-scale structures in the flow field. LES is used to simulate turbulence, and the mechanisms leading to cavitation shedding are investigated at cavitation number of $\sigma = 1.64$. By comparing with experimental results, the accuracy of the multiscale model used in this study is validated. The results reveal that cavitation shedding is primarily induced by the re-entrant jet at the cavitation number of $\sigma = 1.64$. Finally, the clock time per time step when using the VOF-DBM method is 1.17 times longer than that of the VOF method. However, the total simulation clock time with VOF-DBM is 1.2 times shorter due to the larger allowable time step in the VOF-DBM approach.

ACKNOWLEDGEMENTS

This study was funded by the Natural Science Foundation of China (52106155) and the China Postdoctoral Science Foundation (2023M743269).

REFERENCES

[1] Mohan, B., Yang, W., and Kiang Chou, S., 2013, "Fuel injection strategies for performance improvement and emissions reduction in compression ignition engines—A review", *Renewable Sustainable Energy Rev*, Vol. 28, pp. 664–676.

[2] Xuan, T., Maes, N., García-Oliver, J. M., De León-Ceriani, D., Pachano, L., and He, Z., 2022, "Combined experimental and numerical studies on soot characteristics of diesel sprays with split injection strategies", *Combust Flame*, Vol. 246, p. 112384.

[3] Gavaises, M., 2008, "Flow in valve covered orifice nozzles with cylindrical and tapered holes and link to cavitation erosion and engine exhaust emissions", *Int J Engine Res*, Vol. 9, pp. 435–447.

[4] Guan, W., Huang, Y., He, Z., Guo, G., Wang, C., and Thévenin, D., 2024, "Primary breakup of a jet coupled with vortex-induced string cavitation in a fuel injector nozzle", *Phys Fluids*, Vol. 36 (5).

[5] Gavaises, M., Papoulias, D., Andriotis, A., Giannadakis, E., and Theodorakakos, A., 2007, "Link between cavitation development and erosion damage in diesel injector nozzles", *Tech. rep.*, SAE Technical Paper.

[6] Wu, P., Bai, L., Lin, W., and Yan, J., 2017, "Stability of cavitation structures in a thin liquid layer", *Ultrason Sonochem*, Vol. 38, pp. 75–83.

[7] Kadivar, E., el Moctar, O., and Javadi, K., 2018, "Investigation of the effect of cavitation passive control on the dynamics of unsteady cloud cavitation", *Appl Math Modell*, Vol. 64, pp. 333–356.

[8] Oerley, F., Trummler, T., Hickel, S., Mihatsch, M., Schmidt, S., and Adams, N., 2015, "Large-eddy simulation of cavitating nozzle flow and primary jet break-up", *Phys Fluids*, Vol. 27 (8).

[9] Usta, O., Köksal, Ç. S., and Korkut, E., 2023, "A systematic study into the cavitation erosion test for marine propeller materials by cavitating jet technique", *Ocean Eng*, Vol. 284, p. 115252.

[10] Koukouvinis, P., Gavaises, M., Li, J., and Wang, L., 2016, "Large Eddy Simulation of Diesel injector including cavitation effects and correlation to erosion damage", *Fuel*, Vol. 175, pp. 26–39.

[11] Ghahramani, E., Ström, H., and Bensow, R., 2021, "Numerical simulation and analysis of multi-scale cavitating flows", *J Fluid Mech*, Vol. 922, p. A22.

[12] Li, L., Pei, C., Wang, Z., Lin, Z., Li, X., and Zhu, Z., 2024, "Assessment of cavitation erosion risk by Eulerian–Lagrangian multiscale modeling", *Int J Mech Sci*, Vol. 262, p. 108735.

[13] Zwart, P. J., Gerber, A. G., Belamri, T., et al., 2004, "A two-phase flow model for predicting cavitation dynamics", *Fifth International Conference on Multiphase Flow.–Yokohama, Japan.–2004*.

[14] Li, L., Huo, Y., Wang, Z., Li, X., and Zhu, Z., 2021, "Large eddy simulation of tip-leakage cavitating flow using a multiscale cavitation model and investigation on model parameters", *Phys Fluids*, Vol. 33 (9).

[15] Nicoud, F., and Ducros, F., 1999, "Subgrid-scale stress modelling based on the square of the velocity gradient tensor", *Flow Turbul Combust*, Vol. 62, pp. 183–200.

[16] He, Z., Chen, Y., Leng, X., Wang, Q., and Guo, G., 2016, "Experimental visualization and LES investigations on cloud cavitation shedding in a rectangular nozzle orifice", *Int Commun Heat Mass Transfer*, Vol. 76, pp. 108–116.

[17] Pope, S. B., 2000, *Turbulent Flows*, Cambridge University Press.